Computational Materials Design

The effect of Cr alloying on defect migration at Ni grain boundaries

Blas P. Uberuaga[1,*] (iD), Pauline Simonnin[2] (iD), Kevin M. Rosso[2] (iD), Daniel K. Schreiber[3] (iD), and Mark Asta[4,5] (iD)

[1] *Materials Science and Technology Division, Los Alamos National Laboratory, Los Alamos, NM 87545, USA*
[2] *Physical and Computational Sciences Directorate, Pacific Northwest National Laboratory, Richland, WA 99352, USA*
[3] *Energy and Environment Directorate, Pacific Northwest National Laboratory, Richland, WA 99352, USA*
[4] *Department of Materials Science and Engineering, University of California, Berkeley, CA 94720, USA*
[5] *Materials Sciences Division, Lawrence Berkeley National Laboratory, Berkeley, CA 94720, USA*

ABSTRACT

Mass transport along grain boundaries in alloys depends not only on the atomic structure of the boundary, but also its chemical make-up. In this work, we use molecular dynamics to examine the effect of Cr alloying on interstitial and vacancy-mediated transport at a variety of grain boundaries in Ni. We find that, in general, Cr tends to reduce the rate of mass transport, an effect which is greatest for interstitials at pure tilt boundaries. However, there are special scenarios in which it can greatly enhance atomic mobility. Cr tends to migrate faster than Ni, though again this depends on the structure of the grain boundary. Further, grain boundary mobility, which is sometimes pronounced for pure Ni grain boundaries, is eliminated on the time scales of our simulations when Cr is present. We conclude that the enhanced transport and grain boundary mobility often seen in this system in experimental studies is the result of non-equilibrium effects and is not intrinsic to the alloyed grain boundary. These results provide new insight into the role of grain boundary alloying on transport that can help in the interpretation of experimental results and the development of predictive models of materials evolution.

Introduction

Mass transport is of fundamental importance for understanding materials behavior under a wide range of conditions. It has widely been recognized that grain boundaries (GBs) are often important for dictating the transport of atoms in a material. Depending on the material, boundaries can either enhance [1, 2] or even impede [3] transport. Further, GBs are also important for describing radiation damage evolution. They act as sinks for radiation-

---

Handling Editor: M. Grant Norton.

Address correspondence to E-mail: blas@lanl.gov

 Springer

induced defects, facilitating the recombination of interstitials and vacancies [4, 5]. However, critically, those defects do not simply disappear once they encounter a GB—they migrate until they either escape the system, maybe reaching a free surface, or they encounter other defects [6, 7].

Thus, it is imperative that we understand how defects migrate at grain boundaries and atomistic simulations are a crucial tool in providing this understanding. Past work by multiple groups has examined how the atomic structure of GBs impacts both interstitial and vacancy migration [6, 8–14]. However, the vast majority of these simulations has focused on elementally pure systems. In contrast, most materials of practical interest are alloys.

As one example of the importance of understanding the fundamental mechanisms of transport within GBs of alloys, consider recent experiments by Zhou et al. that examined the corrosive behavior of Ni-Cr alloys in contact with FLiNaK molten salt [15]. They found that the salt preferentially attacks the GBs and, further, preferentially leaches out the Cr from the GBs. However, radiation slowed the corrosive process, indicating that mass transport to or along the boundaries countered the leaching process due to the salt. In addition, external factors can lead to changes in the mobility of the boundary itself—so-called diffusion-induced grain-boundary migration (DIGM) [16–19] – which can fundamentally alter the microstructure and chemistry of the GB. To truly understand what drives this composite and coupled behavior, we must better understand how alloying at grain boundaries impacts mass transport.

There have been limited studies of the effects of alloying or chemical segregation on diffusion at GBs. Recently, Koju and Mishin studied the effect of alloying on GB transport in Cu-Ag [20] and Al-Mg [21]. In the first system, they found that alloying with Ag has a complicated impact on mass transport. For example, at low concentrations of Ag (about 1 atomic % or less), Ag slows down transport. However, as concentrations approach 2%, it can, in some cases, induce higher mobilities than in the unalloyed system. In contrast, alloying Al with Mg uniformly reduces the overall rate of mass transport along the GBs. In these studies, they considered only a few types of GBs, but even so, they revealed complex behavior that highlights the need for further interrogation of these effects.

In this work, we follow a similar path as Koju and Mishin to consider the effect of Cr alloying on transport on GBs in Ni. We consider four GBs that are structurally diverse to understand how Cr impacts mass transport as induced by either an interstitial or a vacancy. We consider different levels of Cr to determine the effect of Cr concentration on the atomic mobility. We begin by using semi-grand canonical Monte Carlo to introduce Cr at various concentrations to a set of GBs in Ni. We then use molecular dynamics (MD) to determine the impact of the added Cr on the rate of transport of both interstitials and vacancies. Finally, we discuss the implications of our results in the context of experimental observations of mass transport along GBs.

Methodology

We examine the effect of Cr alloying on mass transport along GBs in Ni. To understand the relationship between GB structure and transport, we study four different GBs with very different character—a symmetric tilt, an asymmetric tilt, a pure twist, and an asymmetric tilt plus twist GB. We have used these same structures in other studies [6, 22]. Our rationale for focusing on only a small but diverse set of GBs is that there is more variation in properties by considering this set rather than a systematic study of one type versus relatively small changes in structure.

The full orientation relationships for these boundaries are provided in Table 1. We use the same atomic structures we used in our previous work [6, 22], relaxing them to the fcc Ni lattice constant. We adopt a slab model in which we have one GB in the center of our structure and frozen atoms far from the boundary. The number of atoms and the dimensions of our structures are also given in Table 1.

We use the angular-dependent interatomic potential of Howells and Mishin [23] to describe the Ni-Cr interactions. This potential was chosen because it reproduces the phase boundaries between fcc and bcc solid solutions reasonably well. All simulations were performed using LAMMPS. To determine Cr concentrations and distributions within each GB, we perform semi-grand canonical Monte Carlo (SGCMC), as described in Ref. [24] and implemented in LAMMPS. SGCMC involves performing standard Metropolis Monte Carlo but on the semi-grand

Table 1 Orientations of the grains in the four GBs considered here, along with the dimensions of the resulting simulation cells (which are periodic in x and y but not z) and the number of atoms in each cell

Boundary	Upper grain			Lower grain			Dimensions (Å)			Number of atoms
	x	y	z	x	y	z	x	y	z	
Symmetric Σ11 tilt	$[32\bar{3}]$	$[101]$	$[\bar{1}31]$	$[3\bar{2}3]$	$[101]$	$[13\bar{1}]$	24.71	24.85	80.32	4020
Asymmetric Σ11 tilt	$[54\bar{5}]$	$[101]$	$[\bar{2}52]$	$[18\bar{1}]$	$[101]$	$[\bar{4}14]$	28.59	24.85	60.93	4020
Σ5 twist	$[30\bar{1}]$	$[103]$	$[010]$	$[301]$	$[\bar{1}03]$	$[010]$	33.34	33.33	88.47	9180
Σ45	$[210]$	$[1\bar{2}0]$	$[001]$	$[01\bar{2}]$	$[5\bar{4}2]$	$[221]$	23.57	23.57	78.34	4050

The definition of upper and lower grain is arbitrary, but here simply refers to the grain above the GB plane and the grain below, as defined by the relative z position. This same convention is used in the figures (e.g. Fig. 2) and the associated discussion in the text

canonical ensemble. Essentially, instead of just considering the energy change associated with swapping two atoms in our structure, as we would in the canonical ensemble, here we consider a combined system that includes our GB structure and the reservoir of elemental species. When we perform a Monte Carlo step, we exchange Ni or Cr in our simulation for the other element in the reservoir. Thus, the energy change upon such a swap is defined by

$$\Delta E = \Delta E^{sc} + \Delta\mu\Delta N \qquad (1)$$

where ΔE^{sc} is the change in energy in our simulation cell upon changing the chemical identity of one atom while ΔN is the number of atoms that were changed (always ±1 in our simulations). In our case, positive ΔN corresponds to Cr being moved from the reservoir to the GB structure. $\Delta\mu$ is the difference in chemical potential between Ni and Cr ($\mu_{Ni} - \mu_{Cr}$) and here is a parameter defining the simulation. (For convenience and simplicity, we will define $\mu = \Delta\mu$ in this paper.) The Metropolis acceptance criterion is then defined by Eq. 1. The energy of the system is minimized after each trial move, before the move is accepted or rejected. We used a low temperature, 10 K, to define the acceptance probability of the Metropolis algorithm, which essentially leads to the acceptance of only those moves that reduce the energy of the system, moving it toward a low energy state. The slab dimensions were held constant as the Cr content was changed during the MC simulation. The chemical potential μ was scanned from roughly −0.025 to 0.4 eV. As μ decreases, the propensity for Cr to be inserted into the structure increases.

We performed a total of 100 MC cycles for each value of the chemical potential and each GB structure, wherein, for each cycle, N_{trial} MC moves were tested, where $N_{trial}=0.1N_{atom}$ and N_{atom} is the number of atoms in the structure, as given in Table 1. In between each cycle, 1000 MD steps with a target temperature of 10 K were performed, to reduce internal strain due to the changing chemical distribution. In the MC simulations, we used the same random number seed for all cases, but given we are interested in finding the "lowest" energy structure, as long as the sampling is thorough, this should not be an issue. Further, because of the low temperature of the MC sampling, all of the solutes reside at the GB in all cases. There are no solutes in the bulk.

Once structures containing Cr were obtained, selected structures were used as the starting point for MD simulations, again using LAMMPS. Again, for these simulations, the slab dimensions were held fixed. We realize this introduces strain into the system, as we are not allowing for thermal expansion, but here we are more interested in trends than absolute numbers and have no reason to expect that the trends will be affected by this constraint. We use the Langevin thermostat with a damping parameter of 100 ps and a time step of 2 fs. All MD simulations lasted 10 ns (5,000,000 time steps). We performed simulations introducing either one extra Ni atom—an interstitial – or removing one Ni atom – creating a vacancy—at the GB to induce transport. For each temperature and defect, five independent simulations were done with a different random seed. (However, as noted below, not all results were used for various reasons.)

To extract the diffusivity and migration energies, we rely upon the Einstein relation and the Arrhenius equation:

$$D = \lim_{t \to +\infty} \frac{<r(t)^2>}{2dt} = D_0 e^{-E_m/k_B T}. \tag{2}$$

Here, D is the diffusion coefficient, $<r(t)^2>$ is the mean-squared displacement (MSD), d is the dimensionality of the problem ($d = 2$ here as migration is confined to the GB plane), t is time, D_0 is the diffusion coefficient prefactor, E_m is the migration energy, k_B is the Boltzmann constant, and T is the temperature. D is extracted from the MSD for a range of temperatures and the slope of $\log(D)$ vs $1/k_B T$ provides E_m.

To extract the MSD from the trajectories, we use a code developed by Keffer [25]. This code implements the time averaging scheme described in Haile [26] via the following equation:

$$<r(\tau)^2> \ \approx \frac{1}{N}\sum_{i=0}^{N-1}[r(i\Delta t + n\Delta t) - r(i\Delta t)]^2. \tag{3}$$

Here, Δt is the smallest time interval in the trajectory, $\tau = n\Delta t$ is the time interval over which the MSD is being calculated as defined by n, $i\Delta t$ is the origin of time for that segment, and N is the number of segments of size n in the trajectory. As n increases, the number of segments of that size decreases, leading to increased statistical noise. Thus, we extract D from the MSD for a small window of τ near to, but not quite at, $\tau = 0$ ns. More specifically, the window over which D was extracted was from 0.8 to 1.6 ns, far from the ballistic regime. The MSD extracted from this code is per atom, and thus, unless otherwise specified, all MSDs and values of D reported here are per atom. This impacts the prefactor D_0 but not the migration energy E_m, which is the quantity we are most interested in.

We are interested in the relative mobility of Cr vs Ni as a function of the Cr content at the boundary, the structure of the boundary, and the nature of the defect introduced. As the defect is confined to the boundary due to the relatively strong segregation energy and the vast majority of the simulation cell is comprised of immobile Ni, we have to define a window over which to extract the relative D_{Ni} vs D_{Cr}, which is, in the end, an arbitrary choice. Here, for a given boundary and a given defect, we define this window by determining the maximal extent of Cr migration normal to the boundary through all simulations for that set of conditions, assuming that this is a reasonable signature of the range of migration of the defect. This definition means that we cannot

easily compare Cr mobility in different boundaries, but for a given boundary, we can compare Cr vs Ni mobility. The resulting values of D are again per atom.

As noted above, we encountered a number of challenges when performing these simulations that required selective use of the simulation results. These challenges are schematically illustrated in Fig. 1 and include:

- Detachment of the defect from the boundary (*DD*): if the defect leaves that plane, it is sampling the bulk. We are explicitly interested here in the mobility of defects along the GB plane, so when this happened, unless the defect very quickly returned to the GB plane, we ignored the resulting trajectory. This limits the simulations to lower temperatures to minimize this behavior.

- Constrained motion (*CM*): in the tilt boundaries, the transport characteristics are very anisotropic. For low temperatures, this means that only one direction is reasonably sampled, and perpendicular directions are not. In such cases, we are unable to reliably decompose the transport into the perpendicular direction.

- Defect trapping (*DT*): in some cases when Cr is present at the GB plane, the Cr can trap the defect, resulting in relatively poor statistics for lower temperatures. This limits us to higher temperatures to overcome trapping.

- Generation of new defects (*MD*): if the temperature is too high, Frenkel pairs can be spontaneously generated at the GB plane, resulting in a higher concentration of defects than intended and complicating analysis. We ignored such trajectories.

- GB motion (*GBM*): particularly for the undoped boundaries, the boundary itself could migrate if the temperature was too high. This complicates the analysis of the defect migration. If the defect followed the boundary, we assumed that the in-boundary migration was still described correctly and used results from such trajectories.

Table 2 provides a summary of the runs performed and the number of trajectories that exhibited the various behaviors described above, along with the final number of trajectories used to extract the MSD.

Finally, we used the visualizing software OVITO [27] to both visualize the trajectories as well

defect detaches   motion constrained   defect trapped   multiple defects   grain boundary moves
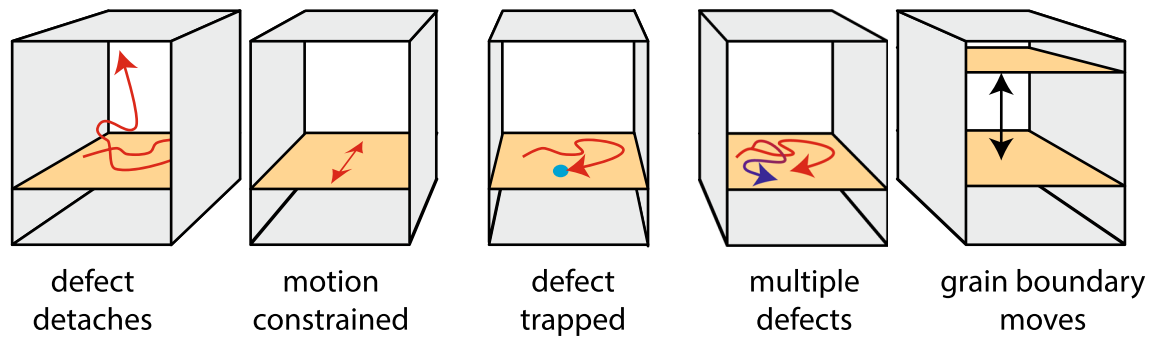
Figure 1 Schematic illustration of the types of complications encountered during our simulations. In order: detachment of the defect from the GB (desegregation); constrained motion along one direction and incomplete sampling in the other; trapping of the defect by the solute; the formation of multiple defects; the migration of the GB itself. Some of these effects are exacerbated at low temperature while the others develop at high temperature, limiting the temperature range over which we can reasonably perform the relevant simulations.

as generate the images of the atomic structures displayed in this manuscript.

Results

The structures of the four boundaries considered here are highlighted in Fig. 2, in which the atoms are colored by their energy, highlighting various structural features at each grain boundary. At the symmetric Σ11 boundary, the tilt axis is very apparent along the y dimension of the structure, though the atoms at the GB plane have energies that are not very different from the matrix. There is greater variation in the asymmetric Σ11 boundary. This structure is characterized by Shockley partials that extend into one grain (the upper grain in the perspective of Fig. 2), providing a wider range of atoms that have a higher energy than the matrix. Further, the atoms at the GB plane have a higher energy than those in the symmetric tilt boundary, suggesting that they might be stronger sites for the segregation of Cr atoms or defects. The Σ5 twist boundary shows a greater density of higher energy sites that span two atomic planes straddling the symmetry plane of the structure. Finally, the Σ45 boundary has the highest energy atoms, which are dispersed across very discrete sites, reminiscent of the misfit dislocation intersections at a semi-coherent boundary. These high energy sites are separated by regions of relatively low energy atoms. As noted above, these four boundaries exhibit very different structural and energetic variations that should lead to very different responses to Cr alloying and defect segregation.

In each of these structures, we performed SGCMC to determine the Cr composition of the boundary as a function of chemical potential. Our primary goal here is to establish different levels of Cr alloying to understand the potential impact on transport. Figure 3 shows the resulting Cr concentration as a function of the chemical potential μ. (Note that this is the number of solutes in the structure per nm^2 of GB area; while in principle this measure does not distinguish between solute atoms at the GB or in the bulk of the grain, since all solutes here reside at the GB, it is a direct measure of solute content at each GB.) We see that, as one would expect, all boundaries exhibit generically similar behavior: as the chemical potential is reduced, more Cr is driven into the structure until, at or just below 0 eV, the entire structure fills with Cr. However, there are also very obvious differences. The high-energy Σ45 boundary, with the highest energy atoms per Fig. 2, is the first to accommodate Cr. That is, it getters Cr for the highest value of μ. Correspondingly, the symmetric Σ11 tilt boundary only begins to fill with Cr at relatively low values of μ. There is thus a strong variation in how Cr segregates to different boundaries—the nature of the boundary is very important for determining the amount of segregated Cr. This is consistent with recent atomistic results highlighting the difference in segregation depending on GB character [28]. Further, the Σ45 boundary also exhibits very discrete plateaus in Cr content, corresponding to the very discrete sites represented in Fig. 2 being filled. The other boundaries tend to display a more gradual filling of Cr versus μ, though they all exhibit plateaus of different degrees. The Σ5 twist boundary, for example, quickly

**Table 2** Summary of all of the simulations done and used to analyze diffusivities

Temperature (K)	Boundary and chemical potential (eV)										
	sym Σ11		asym Σ11		Σ5 twist			Σ45			
	$\mu \gg 0$	$\mu = 0.058$	$\mu \gg 0$	$\mu = 0.175$	$\mu \gg 0$	$\mu = 0.115$	$\mu = 0.035$	$\mu \gg 0$	$\mu = 0.352$	$\mu = 0.252$	$\mu = 0.112$
Interstitials											
800	5	–	–	–	–	–	–	–	–	–	–
900	5	–	–	–	–	–	–	–	–	–	–
1000	5	0 (DT)	–	–	5	5	5	5	5	5	5
1100	5	–	5 (CM)	5 (CM)	–	5	–	5	5	5	5
1200	5	5	–	–	–	–	–	–	–	–	–
1300	5	–	5 (CM)	5 (CM)	5	5	5	5	5	5	5
1400	5	5	5	5	–	–	–	–	–	–	–
1450	–	–	5 (DD)	5 (DD)	–	–	–	–	–	–	–
1500	5	–	5 (DD)	5	5	5	5	5	5	5	5 (DD)
Vacancies											
900	5	5 (DT)	–	–	–	–	–	–	–	–	–
1000	5	5 (DT)	–	–	5	5	5	5	5	5	5
1100	5	5 (DT)	5	0 (DT)	–	–	–	–	–	–	–
1200	5	5 (DT)	5	–	–	–	–	–	–	–	–
1300	5	5 (DT)	3 (MD)	0 (DT)	5	5	5	5	5	5	5
1400	2 (DD)	5 (DD)	5 (DD)	5	–	–	–	5	5	5	5
1450	–	–	4 (DD)	5 (DD)	–	–	–	–	–	–	–
1500	0 (DD)	2 (DD)	5 (DD)	5	5	5	5	5 (DD)	5 (DD)	5	5

In all cases with an entry, 5 simulations were attempted, but only the reported number were deemed suitable for analysis. Parenthetical comments refer to issues for some of the simulations described by Fig. 1 and in the text. Compositions are indicated by the chemical potential μ, which are in eV

Atomic energy distributions

(a) Σ11 sym

(b) Σ11 asym

(c) Σ5 twist

(d) Σ45
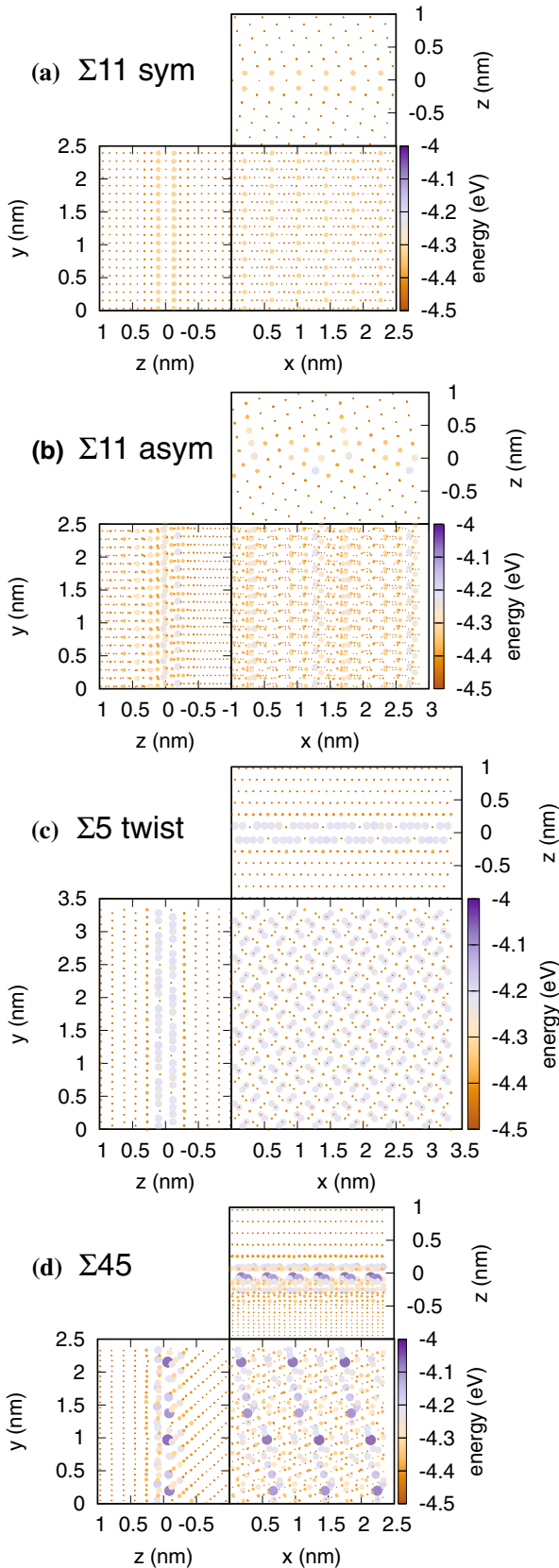
◄**Figure 2** Maps of the energy distribution of atoms within the four pure Ni GB structures considered here: **a** symmetric Σ11 tilt, **b** asymmetric Σ11 tilt, **c** Σ5 twist, and **d** Σ45 asymmetric tilt plus twist. Each boundary is visualized from all sides to provide the most complete picture of the associated energetics. The energy scale is the same for all images to facilitate comparison.

Cr concentration versus chemical potential
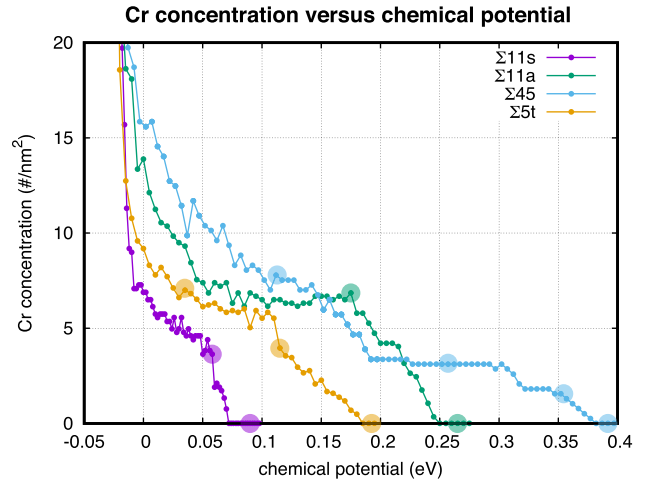
Figure 3 Cr concentration versus the difference in chemical potential (μ) between Ni and Cr for the four boundaries considered here. At high chemical potential, it is unfavorable to introduce Cr into the GB structures. As μ is reduced, more and more Cr is introduced into the GBs. The larger filled circles indicate structures used for subsequent MD simulations.

fills with Cr once a critical value of μ is reached, but then saturates. It is only when μ gets much closer to 0 eV that more Cr can be stuffed into the structure.

For subsequent analysis, several alloyed structures are selected from the structures represented in Fig. 3 and these are highlighted by the filled circles. The actual structure of these alloyed boundaries is presented in Fig. 4. The distribution of Cr at these boundaries is sensitive to the atomic structure of the boundary. Even in the two tilt boundaries, the Cr distribution varies significantly. While Cr is somewhat more dispersed in the symmetric Σ11 tilt, it is strongly aligned along the tilt axis at the asymmetric Σ11 boundary. At the Σ5 twist boundary, Cr is evenly distributed across the boundary plane for both levels of Cr content shown. Finally, for the Σ45 boundary, Cr begins filling discrete and dispersed sites, reflecting the energy landscape revealed in Fig. 2. As more Cr is added, it tends to cluster with the existing Cr, and at the highest levels considered is still not uniformly distributed across the GB plane. Thus, there
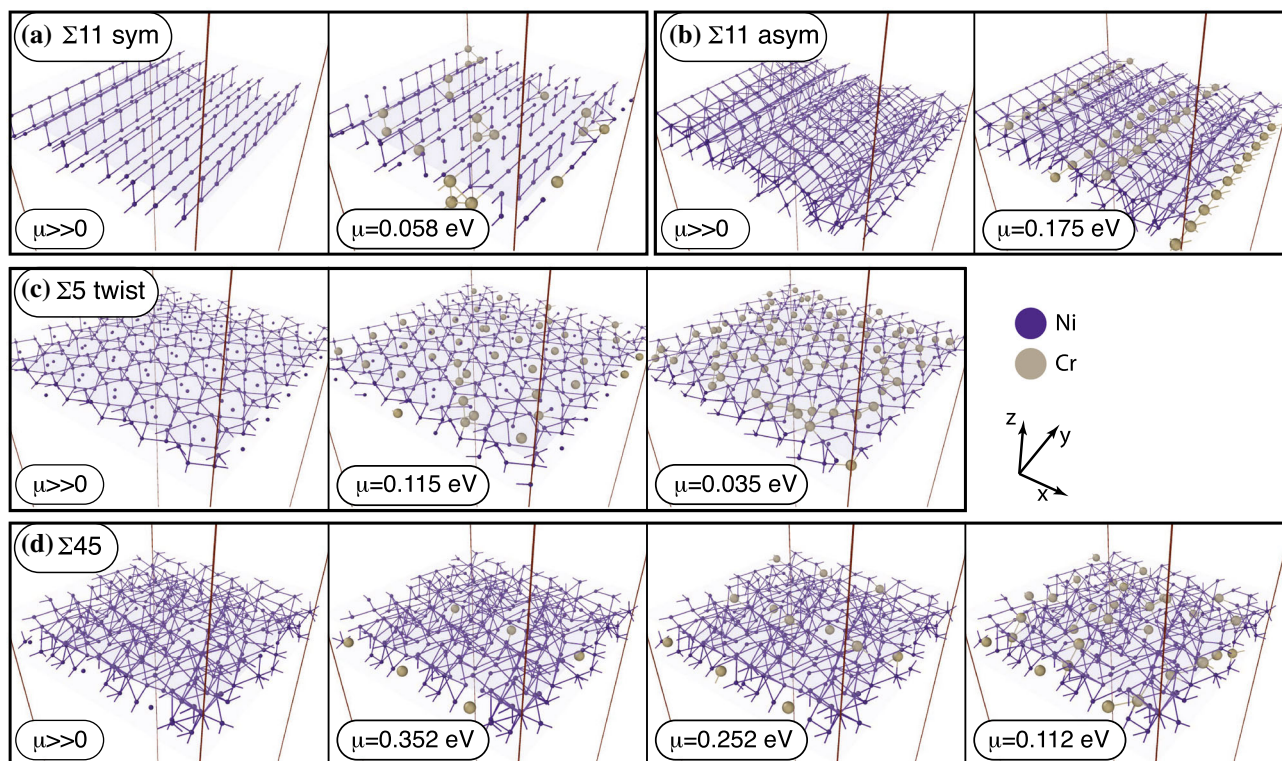
Figure 4 Cr distributions at the four GBs for the compositions highlighted in Fig. 3. Purple spheres indicate Ni, while gold spheres indicate Cr. The "bonds" connecting atoms are shown solely to better visualize the structure, while the vertical lines represent the boundaries of the simulation cell. The dimensions of the cells are given in Table 1.

are a number of different features about how Cr is incorporated into these different boundaries that emphasize the necessity of considering a diverse set of structures.

Finally, before performing dynamical simulations, we calculated the segregation energy of Ni vacancies to the GBs as a function of Cr content, to understand how Cr changes the interaction with defects with the GB. In these calculations, we systematically removed Ni atoms, one-by-one, and minimized the energy to determine the energy of the Ni vacancy as a function of distance from the boundary. The Cr content remained constant in these calculations. By comparing the energy in the bulk region versus at the boundary, we can extract the segregation energy of the vacancy.

Two examples are shown in Fig. 5, for the symmetric $\Sigma 11$ tilt and the $\Sigma 45$ boundaries. Perhaps the more interesting of the two is the symmetric $\Sigma 11$, shown in Fig. 5a. Without Cr, the segregation energy of vacancies to the boundary is -0.26 eV. There are also sites that are just very slightly repulsive, at the mirror plane of the boundary. Upon doping with Cr,

there are two primary effects. First, the attraction to the segregating sites becomes stronger, increasing to -0.34 eV. Maybe more importantly, the repulsive sites become even more repulsive, reaching as high as 0.26 eV. Thus, Cr enhances the heterogeneous nature of the potential energy landscape, potentially complicating the path of defects as they migrate along the boundary plane.

In contrast, as highlighted in Fig. 5b, the changes Cr induces in the vacancy landscape at the $\Sigma 45$ boundary are less dramatic, possibly because that boundary already exhibits a very complex energy landscape. Vacancy segregation energies are already large in the undoped boundary— -1.25 eV—and Cr increases that to -1.30 eV. Cr does create sites that are repulsive to Ni vacancies, but only at the highest levels of doping. In both boundaries, however, the chemical heterogeneity introduced by alloying with Cr increases the heterogeneity of the energy landscape. The other two boundaries, not shown, exhibit similar changes upon Cr alloying.
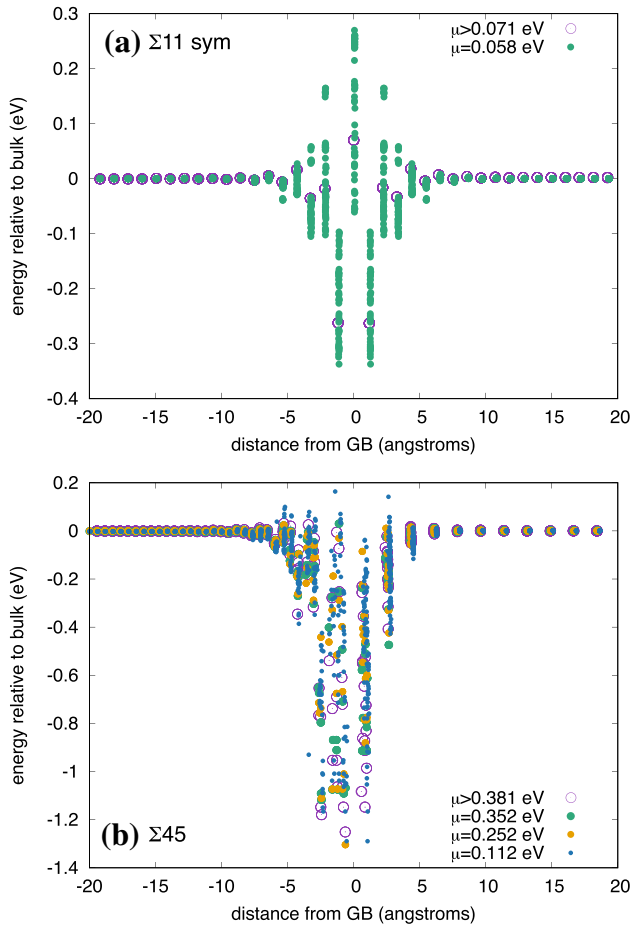
Figure 5 Vacancy segregation energies versus Cr content for the **a** symmetric Σ11 and the **b** Σ45 asymmetric tilt plus twist boundary. The colors of the points refer to different chemical potentials and thus different Cr content, as described in Fig. 3.

Diffusivity of interstitials and vacancies

Figure 6 shows the extracted diffusivity D for both interstitials and vacancies as a function of GB structure, temperature, and chemical potential. Figure 6a provides this data for the symmetric Σ11 tilt boundary. First, comparing the behavior of interstitials versus vacancies in the pure Ni boundary, we find that interstitials migrate much faster. In fact, interstitial migration is almost athermal, with no real temperature dependence in D over the temperature range considered. (Actually, this athermal behavior persists to much lower temperatures, as low as 100 K.) Vacancies, on the other hand, migrate much slower, at least an order of magnitude slower at the highest temperature. If we then consider the effect of Cr, we see that it has essentially no effect on the migration of vacancies, but interstitial migration is
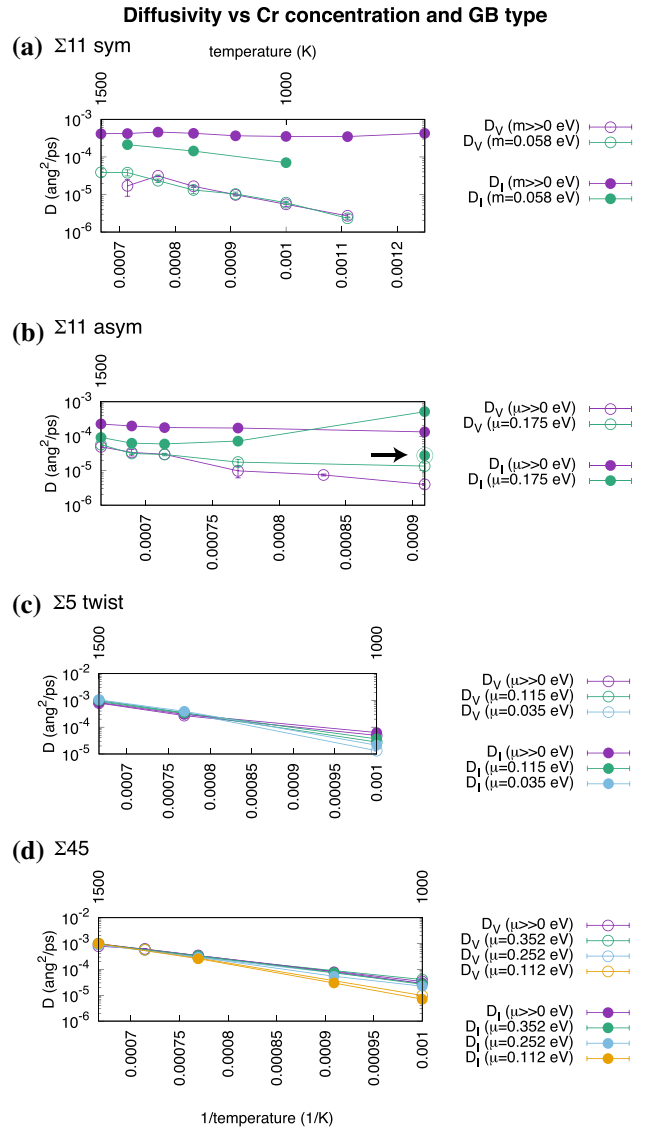
Figure 6 Diffusivity of all atoms, per atom, as a function of Cr content and due to both interstitials and vacancies. **a** symmetric Σ11 tilt, **b** asymmetric Σ11 tilt, **c** Σ5 twist, and **d** Σ45 asymmetric tilt plus twist. Open symbols represent results for vacancies, while filled symbols are for interstitials. Colors represent different levels of Cr content. When error bars are not visible, they are smaller than the size of the points. For the asymmetric Σ11 tilt GB shown in (**b**), an extra point is indicated for interstitial-mediated migration in the Cr-alloyed structure: this structure has a different Cr distribution than the other point for the same conditions, as described in the text.

affected significantly, with a much stronger temperature dependence than in the pure Ni boundary.

Turning to the asymmetric Σ11 tilt boundary, we see a qualitatively similar picture for vacancies: they migrate much slower than interstitials and Cr has

little effect on their mobility, at least at the highest temperatures. However, vacancies tend to get trapped by Cr at lower temperatures, leading to poor statistics and hence their exclusion from the plot. Interstitials exhibit more interesting behavior. In the pure Ni boundary, we again find that they migrate quickly, but there is some temperature dependence; they are not athermal as in the symmetric tilt boundary. As with the symmetric case, Cr slows down interstitial migration, at least at the highest temperatures. Curiously, we see a huge spike in the mobility of atoms in the Cr-alloyed structure at lower temperatures. This is the consequence of the nicely ordered arrangement of Cr as shown in Fig. 4b. We observe that whole columns of Cr ordered along the tilt axis can move almost as one when an interstitial is present. This behavior is not observed at the higher temperatures as the Cr structure is disrupted by perpendicular motion of the atoms; the ordered arrangement becomes broken. To verify this, we have performed simulations at the lower temperature but with the final Cr distribution from the higher temperature. Indeed, we find that diffusion is much lower in this structure, as highlighted in Fig. 6b. Thus, the mobility is sensitive to the detailed distribution of the solute and special arrangements can lead to very high rates of transport.

The $\Sigma 5$ twist and $\Sigma 45$ boundaries exhibit simpler dependencies. There is very little disparity between interstitial and vacancy migration, particularly at the highest temperatures. At the lower temperatures considered, vacancies migrate just slightly faster in the $\Sigma 45$ boundary, while interstitials are slightly faster in the $\Sigma 5$ twist. There is only a modest effect of Cr on the mobility of either defect, with Cr slightly reducing the resulting mass transport due to either defect.

As already mentioned, for the tilt GBs, given their asymmetric boundary structure, there is a strong anisotropy in mass transport along the tilt axis (y in these figures) as opposed to perpendicular to it (the x component). This is highlighted in Fig. 7. There is anisotropy for both interstitials and vacancies, though the anisotropy is greater for interstitials. In the case of a vacancy at the symmetric boundary (Fig. 7a), Cr has little effect on the anisotropy, consistent with the fact that it had little effect on D. In the case of the interstitial (Fig. 7b), only the y component—the component along the tilt axis—is impacted
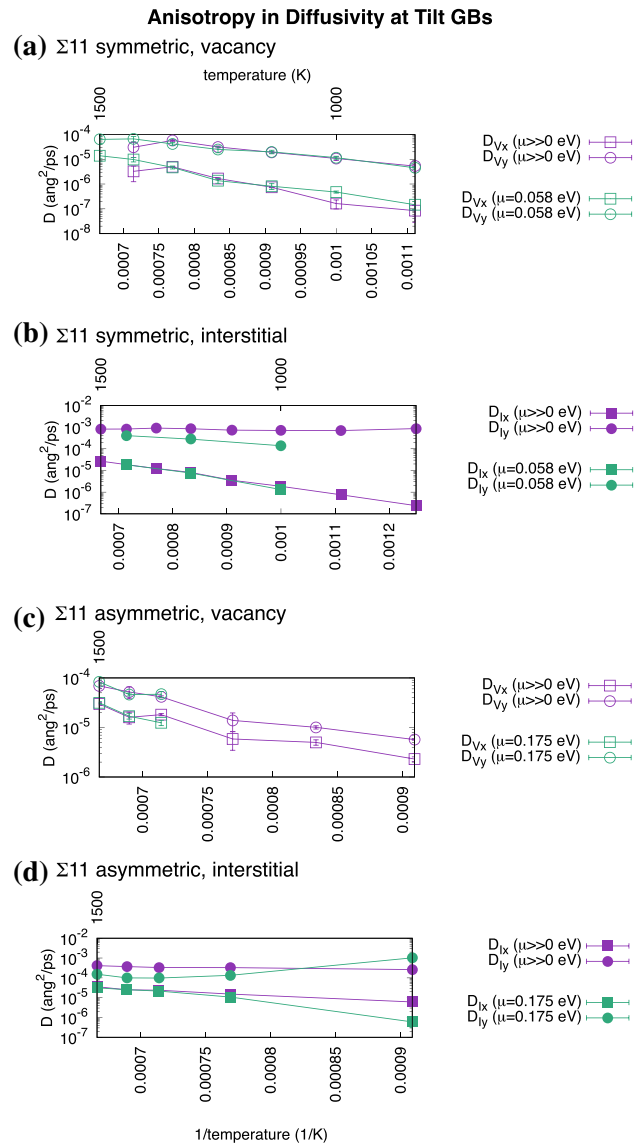
Figure 7 Anisotropy in D for the two pure tilt boundaries: **a** vacancy-mediated migration at the symmetric $\Sigma 11$, **b** interstitial-mediated migration at the symmetric $\Sigma 11$, **c** vacancy-mediated migration at the asymmetric $\Sigma 11$, and **d** interstitial-mediated migration at the asymmetric $\Sigma 11$. In (**a**), D_{Vx} at the highest temperatures experienced detachment, and hence the shift to lower values.

by the Cr. The perpendicular component, already relatively slow, is unaffected by the presence of Cr.

The behavior is essentially the same at the asymmetric tilt boundary, as highlighted in Fig. 7c, d. The vacancy exhibits anisotropic migration that is unaffected by Cr. The transport of interstitials along the tilt axis is reduced by the presence of Cr, except for lower temperatures where the aligned Cr columns can quickly migrate. In fact, the results in Fig. 7d
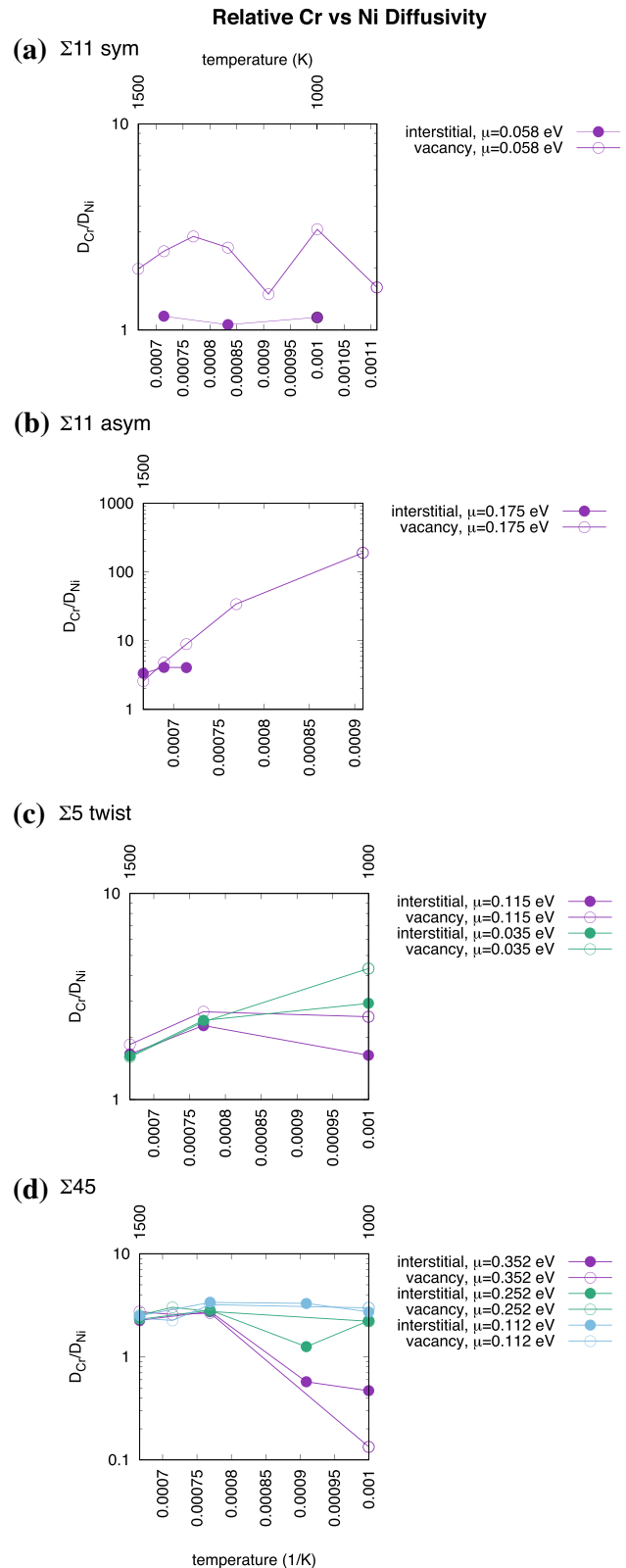
Figure 8 Relative diffusivity of Cr vs Ni at the four GBs—**a** ▶ symmetric Σ11 tilt, **b** asymmetric Σ11 tilt, **c** Σ5 twist, and **d** Σ45 asymmetric tilt plus twist—as a function of defect type and Cr content.

highlight how it is specifically transport along the tilt axis that is increased by the special Cr distribution, with a corresponding drop in the perpendicular component which we attribute to less complete sampling of transport along that direction as the simulation is dominated by transport along the tilt axis.

Finally, it is valuable to understand whether Cr or Ni is migrating faster at these boundaries as a consequence of the presence of the defect. Figure 8a shows the relative diffusivity of Cr as compared to Ni for the symmetric Σ11 tilt boundary. In this case, interstitials move Cr and Ni at essentially the same rate, regardless of temperature, while vacancies tend to accelerate Cr transport over Ni transport by a modest factor of 2 or less. (Note that, in these simulations, we always observe interstitials to migrate via the interstitialcy mechanism, in which atoms are displaced from the lattice during migration, changing the identity of the interstitial as migration proceeds.) The data are particularly noisy because of error bars on the measurements of both D_{Cr} and D_{Ni}; however, it is clear that the relative mobility of the two elements is very similar at this boundary.

Perhaps surprisingly, given how similarly the two tilt boundaries have behaved as described by other measures, in the case of the relative diffusivity of Cr and Ni, the asymmetric Σ11 boundary exhibits some unique behavior. Interstitials tend to enhance Cr diffusivity over Ni by a factor of 2–3 for the temperatures considered. (We have excluded those cases where the Cr distribution led to particularly high mobilities in this analysis.) However, there is a much greater disparity for vacancies that is strongly temperature dependent. At the lowest temperature shown—1100 K—vacancies induce mobility of Cr that is almost 200 times as great as Ni. Thus, at least for some boundaries, there is a large chemical dependence in the transport of elements that depends on the defect under consideration.

The overall variation with chemistry we see for the Σ5 twist is again rather modest, never more than a factor of 4–5. However, there is a slight temperature dependence, particularly for the vacancy, with

Relative Cr vs Ni Diffusivity

(a) Σ11 sym

interstitial, μ=0.058 eV
vacancy, μ=0.058 eV

(b) Σ11 asym

interstitial, μ=0.175 eV
vacancy, μ=0.175 eV

(c) Σ5 twist

interstitial, μ=0.115 eV
vacancy, μ=0.115 eV
interstitial, μ=0.035 eV
vacancy, μ=0.035 eV

(d) Σ45

interstitial, μ=0.352 eV
vacancy, μ=0.352 eV
interstitial, μ=0.252 eV
vacancy, μ=0.252 eV
interstitial, μ=0.112 eV
vacancy, μ=0.112 eV

greater relative transport of Cr at low temperatures, at least for the higher Cr content boundary. For the case with a lower Cr content, the difference at lower temperature is smaller, less than a factor of 3. Finally, there is no big difference between the transport in different chemical species induced by vacancies or interstitials; as for the total D, the behavior for both defects is similar.

Yet another type of behavior is exhibited by the Σ45 boundary, as shown in Fig. 8d. For the highest Cr content, there is little chemical dependence—maybe a factor of 2 faster transport of Cr compared to Ni—nor any big difference in transport induced by interstitials as compared to vacancies. However, for lower Cr content, we find that Cr actually migrates slower than Ni for both interstitials and vacancies, in contrast to all of the other boundaries considered. For vacancies, the effect is almost a factor of 10 at 1000 K. This suggests that Cr, trapped at the high energy sites in this boundary structure, is not easily dislodged by the passing defects.

Effective migration energies

From the diffusivities in Fig. 6, we extract the effective migration energy of species due to vacancies and interstitials; these are reported in Table 3. We note that, for the Cr-loaded asymmetric Σ11 tilt boundary, we are not able to extract meaningful numbers for either defect. In the case of the vacancy, for the data shown in Fig. 6b, there is seemingly no effect of Cr on the diffusivity of the vacancy. However, if we fit an exponential to the data, we find a very different slope as compared to the unalloyed boundary and this is because the data do not extend to low enough temperatures for the Cr-loaded case. If we add lower temperature data, which are plagued by poor statistics due to trapping of the vacancy by the Cr, we obtain very different slopes depending on which points are included. We thus refrain from reporting a value, but suspect that the migration energy in this case is very similar to the pure Ni boundary.

Similarly, we have difficulties extracting a migration energy for interstitial mediated migration in the same boundary, though, in this case, the reason is different. Because of the very fast migration associated with the aligned Cr, the resulting diffusivity versus inverse temperature is non-Arrhenius; the

Table 3 Migration energies E_m extracted from the diffusivity plots in Fig. 6 for the four GBs as a function of both composition (μ, in eV) and defect type

Defect	sym Σ11		asym Σ11		Σ5 twist			Σ45			
	$\mu \gg 0$	$\mu = 0.058$	$\mu \gg 0$	$\mu = 0.175$	$\mu \gg 0$	$\mu = 0.115$	$\mu = 0.035$	$\mu \gg 0$	$\mu = 0.352$	$\mu = 0.252$	$\mu = 0.112$
Vacancy	0.63 ±0.04	0.57 ±0.04	0.92 ±0.04	–	0.72 ±0.06	0.90 ±0.01	1.08 ±0.10	0.88 ±0.02	0.88 ±0.07	0.90 ±0.02	1.16 ±0.06
Interstitial	0.03 ±0.02	0.31 ±0.03	0.20 ±0.07	–	0.69 ±0.09	0.86 ±0.01	1.00 ±0.05	0.90 ±0.01	0.91 ±0.01	0.96 ±0.02	1.23 ±0.05

diffusivity is much higher at lower temperature where the Cr remains aligned. Thus, with the data at hand, it is meaningless to extract a migration energy.

For the other boundaries, we are able to extract reasonable values of the effective migration energy. For the symmetric $\Sigma11$ tilt boundary, as noted, interstitials diffuse almost athermally along the tilt axis when no Cr is present, with an extremely small migration energy of 0.03 eV. This increases by an order of magnitude with Cr is present to 0.31 eV, still reasonably fast, but slower than interstitial self-diffusion in the bulk [29, 30]. Vacancy migration is hardly impacted by the presence of Cr: in the pure case, we find a value of 0.63 eV, while in the doped case, we extract a value of 0.57 eV. The difference may be due to a slight dip in D in the undoped case at the highest temperature, where our statistics are relatively poor and the trajectory, even in the cases included in the evaluation of D, may have some influence of the vacancy detaching from the GB plane.

The other two boundaries, which both have a twist component, behave rather similarly. For both the vacancy and the interstitial in the $\Sigma5$ twist, we find a similar migration energy in the pure Ni boundary—0.72 and 0.69 eV, respectively—that systematically increases as the Cr content increases. For the highest concentration, we find migration energies of 1.08 and 1.00 eV for the vacancy and the interstitial, respectively, thus indicating a significant slowing down of overall rates of transport as Cr is introduced into the boundary plane.

The $\Sigma45$ boundary behaves similarly, though a critical amount of Cr is needed before transport is slowed. For the smallest Cr content, where only the deepest traps are filled, neither the vacancy nor the interstitial are affected. However, as more Cr is included, the barriers increase, from pristine values of 0.88 and 0.90 eV for the vacancy and interstitial, respectively, to 1.16 and 1.23 eV.

Thus, overall, we tend to find that, with the exception of the special arrangements in the asymmetric $\Sigma11$ tilt boundary, Cr slows down the migration of species at these diverse boundary structures. That is, regardless of the detailed atomic structure, Cr has a similar qualitative impact: an increase in the effective migration energy for transport.

Discussion

Summarizing our key results, we find that

- Cr tends to reduce the mobility of atoms due to both interstitial and vacancy migration
- This effect is greatest for interstitial migration along the tilt axis of tilt GBs
- For specific arrangements of Cr in the asymmetric tilt boundary, Cr mobility can be extremely high
- Cr tends to migrate moderately faster than Ni with the exception of the $\Sigma45$ boundary, in which the behavior is non-monotonic with both Cr content and temperature
- Cr reduces the mobility of GBs themselves (this is a point we will discuss below)

As Cr is added to a GB, there is a tendency for vacancies (Fig. 5), and presumably interstitials, to bind more strongly to the boundary. This indicates an attraction between Cr and the defect, suggesting that defect mobility will be hindered because the defect is less able to freely migrate in the boundary plane. Further, as the defect and Cr are associated, this suggests that, when the defect does move, Cr will more likely be nearby and benefit from that motion. This scenario is born out by our simulations, which indicate that overall atomic mobility is reduced when Cr is added to the boundary, though Cr tends to migrate faster than Ni.

This result is in contrast to MD studies of diffusivity in bulk Ni-Cr alloys, which found that increasing Cr concentrations led to higher Ni self-diffusion rates [31]. Here, we find the opposite result, that generally overall transport is slowed by the addition of Cr. That study used a different potential, and it is possible the potential is the source of the difference. Assuming that the potentials would predict similar behavior, we turn to other potential origins of this difference. Of course, GBs might behave fundamentally differently than in the bulk, and past work has shown how migration rates of individual defects can be slower at boundaries than in the bulk [6]. Further, the Cr distribution is very different in the two scenarios. In the bulk, it is dispersed randomly, while in the current boundary studies, it is concentrated at the boundary, often forming relatively dense structures. Thus, we might expect significant differences in behavior even if the potentials were in perfect agreement. We do find agreement

with that previous study in that, generally, Cr vacancy-mediated transport is faster than Ni transport (though the $\Sigma 45$ boundary is an exception), suggesting that the two potentials describe the system in a similar manner.

The impact of Cr is most dramatic at the tilt boundaries. In the absence of Cr, interstitial migration along the tilt axis is very fast, almost athermal, consistent with our previous work on Cu [6]. In particular, the anisotropy exhibited by interstitials at these tilt boundaries is reduced, but not eliminated, by the presence of Cr. Cr disrupts the fast interstitial migration pathways, leading to overall slower migration along the tilt axes. This effect is much weaker, or even non-existant, for vacancies, even though they also exhibit anisotropies. It is the interstitialcy, almost crowdion-like pathways of interstitials, that is most disrupted.

Though we have not made any attempt to quantify it, another important observation from our simulations is that, while in the unalloyed boundaries we often observe significant migration of the boundaries themselves at elevated temperature, once Cr is added, that mobility essentially disappears. (We note that the mobility of the undoped boundary is inherent to the structure, observed even when no defect is added to the structure.) Thus, Cr imposes a significant pinning effect on these boundaries. This is most pronounced for the two boundaries that have a twist component; for the two tilt boundaries, we observe little GB migration regardless of Cr content. However, for those boundaries that do exhibit high mobility in the pure Ni case, Cr almost completely eliminates that mobility on the time scales of our simulations.

Another interesting observation is that, in certain cases, Cr can greatly enhance the mobility of atoms at the GB, at least when interstitials are present. This enhanced mobility only occurs at the asymmetric $\Sigma 11$ tilt boundary and only when the Cr is well aligned along the tilt axis. As highlighted in Fig. 6b, when that arrangement is disrupted, the mobility drops to much lower levels. There is an energetic driving force for the Cr to align, but of course entropy favors a more disordered structure. We cannot say anything about how prevalent such arrangements might be, but when they do exist, they can greatly enhance transport.

Our results indicate that solute and solvent transport is sensitive to both the GB character and the local arrangement of Cr, as emphasized by the extremely high mobility observed in the asymmetric $\Sigma 11$ boundary. These results are generally consistent with recent experimental results by Gheno et al. [32], who found transport varied even along one GB—presumably because of a change of structure—and that some boundaries exhibited extremely high levels of transport. As suggested in that work, the overall diffusion of e.g. Cr at these boundaries is a combination of solute segregation, defect content, and defect mobility within each GB, all of which are sensitive to the GB character. Gheno et al. suggest that changes in transport rates along a boundary might be due to fluctuations in structure, but our results suggest variations in Cr content could also be responsible, though only in very special cases.

It is worth discussing these results in the context of experimental observations regarding DIGM and GB attack by molten salts and high temperature water or gas. Past experiments have revealed that, upon corrosion, Cr is preferentially leached out of GBs toward the reaction front and the boundaries themselves can migrate, leaving behind a Cr-poor region [19]. Our results suggest that the enhanced leaching of Cr is not due to any enhanced mobility of atoms when Cr is present, compared to when no Cr is present (neglecting any changes in defect concentrations). That is, it is rather driven by the thermodynamics of Cr solution in the corrosive liquid and the strong concentration gradients that would result. Our results do suggest that, once Cr leaches from the GB, the GB could then have higher mobility and start to migrate, possibly accounting for the DIGM zone observed in experiment. Thus, we might speculate that Cr diffusion itself does not lead to the migration of the boundary, but rather that the depletion of Cr allows the boundary to migrate and that it will again become immobile when it encounters Cr.

Schreiber et al. [33] have previously discussed how the amount of Cr transport needed to explain DIGM in Ni-5Cr alloys is much higher than expected from literature measurements of GB transport, leading them speculate there must be significant vacancy injection due to oxidation in the material. This is consistent with our results in that Cr mobility is not significantly faster along the GB than Ni and thus there must be some other origin of the enhanced transport observed there. This conclusion is also supported by the results of Gheno et al. [32], who found Arrhenius behavior in the transport,

suggesting that the equilibrium behavior is as expected and other factors must be driving the enhanced mobilities.

It has also been shown [15] that radiation damage can slow the corrosive process in Ni-Cr alloys in certain situations. One of the key impacts of radiation damage is the creation of interstitials. If one assumes that the presence of interstitials is the unique signature of the radiation damage (forgetting for a moment that a supersaturation of vacancies is also created), then we should examine how interstitial mobility differs from vacancy mobility at these boundaries. Here, the story is very dependent on the boundary structure. For tilt boundaries, interstitials always migrate much faster than vacancies. However, for the boundaries with twist components, that is no longer true, and the two defects have very similar mobility. Since pure tilt boundaries are likely the minority in any real material, we would thus conclude that any impact of radiation damage is not directly related to mass transport at the boundaries themselves. Rather, it seems more likely that mass flow from the bulk to the GB is more relevant [34].

When placing our results in context with the prior literature, we conclude that the extremely high levels of transport exhibited in some experimental studies of Ni-Cr GBs must be a consequence of highly non-equilibrium processes. The high mobilities observed there are not a consequence of any intrinsic enhancement of transport due to the presence of Cr. We only observe such behavior for one very special and limited case. More general GBs, as represented here by the $\Sigma45$ boundary, exhibit only modest changes in transport rates when Cr is introduced. We do find, as shown in Fig. 5, that Cr can lead to enhanced defect content at the boundary, but the effect does not seem to be sufficient to explain the experiments, and any enhancement is particularly weak for the more general grain boundary. Thus, this leads us to conclude that other non-equilibrium processes, possibly vacany injection due to Cr leaching, are the source of the enhanced transport seen in experiments. That said, while generally Cr and Ni transport rates are similar in most of our simulations, there is at least one case—the asymmetric $\Sigma11$ boundary—where Cr migrates much faster when vacancies are present. It is possible that certain boundaries would exhibit the high transport rates observed in experiment, but most seem not to.

Comparing to the recent work by Koju and Mishin [20, 21], which examined the effects of Mg doping on transport at GBs in Al and Ag alloying on transport along GBs in Cu, our results for the Ni-Cr system are in qualitative agreement. They found that Mg reduces transport at GBs in Al, similar to what we conclude for Cr in Ni. In contrast, Ag alloying in Cu did not result in such a simple change in transport, with D initially decreasing and then increasing with Ag content. However, they found that Cu transport generally slowed with Ag additions. They note that they only considered one GB, and as we have seen here, the details do depend on the GB structure. We have also seen special cases where transport can be different or accelerated compared to typical scenarios, depending on the solute distribution. That said, as a whole, our results are generally consistent with the behavior seen for these other two alloyed systems, suggesting that alloying generally slows transport at GBs.

Finally, we should note some limitations of this study. First, all of our MD simulations start with Cr distributions that are found from 10 K SGCMC simulations. In reality, the Cr distribution would, of course, be temperature dependent and we should perform the SGCMC at the temperature of the MD simulations to get a more representative distribution. And, indeed, we have seen cases where the specific distribution matters a great deal. However, we also see that, for the most part, the log of the diffusivity behaves smoothly with inverse temperature, and tracks similarly to the unalloyed cases, suggesting that those simulations are not overly sensitive to the Cr distribution (or that the distribution quickly adjusts to the temperature of the simulation). Thus, we suspect that this is not making a huge impact on our results. Finally, we have only considered the change in migration due to a single defect induced by the addition of Cr. The changing chemical composition will also change the thermodynamic concentration of defects, an effect we have not considered here.

Second, while we have chosen a set of GBs to study that are structurally diverse, they still represent a very small fraction of the near-infinite GB possibilities. More importantly, our set is likely too small to draw many general conclusions. One could imagine that, with a larger dataset, it would be possible to learn, for example via materials informatics approaches [35, 36], properties that could lead to general models appropriate for the mesoscale. It would be

extremely valuable to have a "law" that relates mobility to Cr content and GB structure. Our results, while providing important insight into that relationship, are not sufficient to construct such a law.

Finally, there are other considerations that would be important for future work. For example, we have explicitly limited our study to transport within the boundary plane. However, as noted above, transport to and from the boundary is also important for understanding the chemical evolution of these materials under extreme conditions. Further, as we have shown in the past [6, 37], defects do not necessarily exist as isolated point defects within GBs; they cluster, and that clustering impacts their mobility. Finally, there have only been a few studies now explicitly examining the impact of GB alloying on mass transport. We need more studies of a wider range of chemical systems to draw more general conclusions on this relationship.

Conclusion

To conclude, we have used molecular dynamics simulations to examine the impact of Cr alloying on mass transport at GBs due to both interstitials and vacancies. We find that, generally, Cr tends to increase the migration energy of defects, or decrease the overall mobility of atoms within the boundary plane. At the same time, Cr mobility tends to be higher than Ni mobility at most boundaries, suggesting a complicated relationship between the defects and the alloying element. The biggest impact is observed at pure tilt boundaries, in which preferential migration of interstitials along the tilt axis is significantly impact by Cr. However, we also observe that there are special arrangements of Cr that can lead to exceptionally high transport rates. Finally, we find that Cr tends to eliminate the mobility of some GBs themselves, and conversely Cr depletion via corrosive leaching may promote boundary migration. Overall, our results provide new insight into the impact of alloying on GB transport and help in the interpretation of experimental observations of molten salt corrosion at GBs.

Acknowledgements

Declarations

References

[1] Balluffi R (1982) Grain boundary diffusion mechanisms in metals. Metall Trans B 13:527

[2] Atkinson A (1984) Diffusion along grain boundaries and dislocations in oxides, alkali halides and carbides. Solid State Ionics 12:309

[3] Lin Y-Y, Yong AXB, Gustafson WJ, Reedy CN, Ertekin E, Krogstad JA, Perry NH (2020) Toward design of cation transport in solid-state battery electrolytes: structure-dynamics relationships. Curr Opin Solid State Mater Sci 24:100875

[4] Singh BN (1974) Effect of grain size on void formation during high-energy electron irradiation of austenitic stainless steel. Philos Mag: J Theor Exp Appl Phys 29:25

[5] Beyerlein I, Caro A, Demkowicz M, Mara N, Misra A, Uberuaga B (2013) Radiation damage tolerant nanomaterials. Mater Today 16:443

[6] Uberuaga BP, Vernon LJ, Martinez E, Voter AF (2015) The relationship between grain boundary structure, defect mobility and grain boundary sink efficiency. Sci Rep 5:1

[7] Dunn A, Dingreville R, Martínez E, Capolungo L (2016) Identification of dominant damage accumulation processes at grain boundaries during irradiation in nanocrystalline α-Fe: A statistical study. Acta Mater 110:306

[8] Balluffi R, Kwok T, Bristowe P, Brokman A, Ho P, Yip S (1981) Determination of vacancy mechanism for grain boundary self-diffusion by computer simulation, Tech. Rep., Massachusetts Inst. of Tech., Cambridge (USA)

[9] Kwok T, Ho P, Yip S, Balluffi R, Bristowe P, Brokman A (1981) Evidence for vacancy mechanism in grain boundary diffusion in bcc iron: a molecular-dynamics study. Phys Rev Lett 47:1148

[10] Nomura M, Lee S-Y, Adams JB (1991) Vacancy diffusion along twist grain boundaries in copper. J Mater Res 6:1

[11] Nomura M, Adams JB (1992) Self-diffusion along twist grain boundaries in Cu. J Mater Res 7:3202

[12] Nomura M, Adams JB (1995) Interstitial diffusion along twist grain boundaries in Cu. J Mater Res 10:2916

[13] Mishin Y, Herzig C (1999) Grain boundary diffusion: recent progress and future research. Mater Sci Eng, A 260:55

[14] Starikov S, Mrovec M, Drautz R (2020) Study of grain boundary self-diffusion in iron with different atomistic models. Acta Mater 188:560

[15] Zhou W, Yang Y, Zheng G, Woller KB, Stahle PW, Minor AM, Short MP (2020) Proton irradiation-decelerated intergranular corrosion of Ni–Cr alloys in molten salt. Nat Commun 11:1

[16] Balluffi R, Cahn J (1981) Mechanism for diffusion induced grain boundary migration. Acta Metall 29:493

[17] Pan J, Balluffi R (1982) Diffusion induced grain boundary migration in AuCu and AuAg thin films. Acta Metall 30:861

[18] King A (1987) Diffusion induced grain boundary migration. Int Mater Rev 32:173

[19] Volpe L, Burke MG, Scenini F (2020) Correlation between grain boundary migration and stress corrosion cracking of alloy 600 in hydrogenated steam. Acta Mater 186:454

[20] Koju R, Mishin Y (2020a) Relationship between grain boundary segregation and grain boundary diffusion in Cu–Ag alloys. Phys Rev Mater 4:073403

[21] Koju R, Mishin Y (2020b) Atomistic study of grain-boundary segregation and grain-boundary diffusion in Al–Mg alloys. Acta Mater 201:596

[22] Bai X-M, Vernon LJ, Hoagland RG, Voter AF, Nastasi M, Uberuaga BP (2012) Role of atomic structure on grain boundary-defect interactions in Cu. Phys Rev B 85:214103

[23] Howells C, Mishin Y (2018) Angular-dependent interatomic potential for the binary Ni–Cr system. Model Simul Mater Sci Eng 26:085008

[24] Sadigh B, Erhart P, Stukowski A, Caro A, Martinez E, Zepeda-Ruiz L (2012) Scalable parallel Monte Carlo algorithm for atomistic simulations of precipitation in alloys. Phys Rev B 85:184203

[25] Keffer DJ http://utkstair.org/clausius/docs/mse614/index.html

[26] Haile J (1992) Molecular dynamics simulation: elementary methods, monographs in physical chemistry series. Wiley, London

[27] Stukowski A (2010) Visualization and analysis of atomistic simulation data with OVITO-the Open Visualization Tool, Modelling and Simulation in Materials Science and Engineering 18, ISSN 0965-0393

[28] Barr CM, Foiles SM, Alkayyali M, Mahmood Y, Price PM, Adams DP, Boyce BL, Abdeljawad F, Hattar K (2021) The role of grain boundary character in solute segregation and thermal stability of nanocrystalline Pt-Au. Nanoscale 13:3552

[29] Zhao P, Shimomura Y (1999) Molecular dynamics calculations of properties of the self-interstitials in copper and nickel. Comput Mater Sci 14:84

[30] Poletaev G, Starostenkov M (2010) Contributions of different mechanisms of self-diffusion in face-centered cubic metals under equilibrium conditions. Phys Solid State 52:1146

[31] Simonnin P, Schreiber DK, Rosso KM (2021) Predicting the temperature dependence of self-diffusion behavior in Ni–Cr alloys via molecular dynamics. Mater Today Commun 26:101982

[32] Gheno T, Jomard F, Desgranges C, Martinelli L (2019) Grain boundary diffusion of chromium in polycrystalline nickel studied by SIMS. Materialia 6:100283

[33] Schreiber DK, Olszta MJ, Bruemmer SM (2014) Grain boundary depletion and migration during selective oxidation of Cr in a Ni-5Cr binary alloy exposed to high-temperature hydrogenated water. Scripta Mater 89:41

[34] Barr CM, Barnard L, Nathaniel JE, Hattar K, Unocic KA, Szlurfarska I, Morgan D, Taheri ML (2015) Grain boundary

character dependence of radiation-induced segregation in a model Ni–Cr alloy. J Mater Res 30:1290

[35] Rosenbrock CW, Homer ER, Csányi G, Hart GL (2017) Discovering the building blocks of atomic systems using machine learning: application to grain boundaries. NPJ Comput Mater 3:1

[36] Sharp TA, Thomas SL, Cubuk ED, Schoenholz SS, Srolovitz DJ, Liu AJ (2018) Machine learning determination of atomic dynamics at grain boundaries. Proc Natl Acad Sci 115:10943

[37] Bai X-M, Voter AF, Hoagland RG, Nastasi M, Uberuaga BP (2010) Efficient annealing of radiation damage near grain boundaries via interstitial emission. Science 327:1631

Publisher's Note Springer Nature remains neutral with regard to jurisdictional claims in published maps and institutional affiliations.